Optimization of Voltages Combination for Gold-based Contrast Agents below K-edges in Dual-energy Micro-CT

Yuan Yuan[1], Yanbo Zhang[2], Hengyong Yu[2,*]

1. *Department of Physics and Applied Physics, University of Massachusetts Lowell, Lowell, MA, 01854 USA*
2. *Department of Electrical and Computer Engineering, University of Massachusetts Lowell, Lowell, MA, 01854, USA*

* Corresponding author, email:hengyong-yu@ieee.org

***Abstract*—Dual-energy micro- Computed Tomography provides high resolution for non-invasive images at low cost. It can determine the concentrations of constituent materials in a mixture. Taking advantage of K-edge, gold-based agents contribute to improve the contrast of some physiological tissues with low natural contrast. Because the K-edge of gold (80.7 kVp) is excessively high, the anatomical structures could not be identified clearly in *in vivo* small animal experiments. In this study, the voltage combination below K-edge is optimized to differentiate cortical bone, soft tissue and gold. To further improve the accuracy, the reconstructed dual-energy images are filtered using a joint bilateral filtration. Based on the quantitative analysis of material decomposition, the optimized voltage pair are 45kVp and 65kVp. Our results could provide practical guidance for the design of *in vivo* small animal experiments using gold nanoparticles as contrast agents.**

Keywords—material decomposition; gold nanoparticles; contrast agents; scanning voltage; joint bilateral filtraion.

I. INTRODUCTION

Micro-computed tomography (micro-CT) is an efficient and widely accepted tool for preclinical research, and it has been extensively used in non-invasive small animal experiment[1]. The development of exogenous contrast agents contributes to highlighting physiological features with low natural contrast in micro-CT images [2]. In 2006, as new and promising x-ray contrast agents, Gold (Au) nanoparticles were used in *in vivo* experiments [3]. As an effective experimental x-ray contrast agent, gold has been reported to overcome many obstacles of traditional iodine-based contrast agents [4]. Compared with the well-known iodine, gold provides about 2.7 times greater contrast per unit weight due to its high atomic number and high photoelectric photon absorption[3]. Gold also takes advantage of its low toxicity and biocompatibility[5]. The effectiveness of gold as a contrast agent depends on not only their physical properties, but also the scanning conditions. X-ray tube voltage is a major determinant of contrast. Gold absorbs x-rays strongly in the 80-120keV range since the K-edge of gold is 80.7 keV. Hence gold can provide greater contrast when it is scanned at 120kV and 80kV [6].

Despite of advancements in new contrast agents, it is still difficult to segment image based on grey-scale signal intensity alone because different materials may share similar grey-scale intensity values in single-energy CT images. As a result, the dual-energy CT imaging (DECT) was developed, where an object is scanned using two energy spectra with different voltage settings. The main advantage of DECT over conventional CT is the photon energy dependence of the linear attenuation coefficients. Due to the incorporation K-edge, dual-energy CT images can be decomposed into different material basis images[7]. DECT also has a capability to determine the concentration of constituent materials in mixture. The obtained basis material images depend on the linear attenuation coefficients and dual-energy projection data acquisition[8]. Material decomposition can be performed either in projection-domain [9] or image-domain [10-13].

In this study, we will work in image-domain, and the linear attenuation coefficients derived from reconstructed images at low- and high-energies are expressed as a linear combination of the pixel values in the images of two basis materials [10]. Thus, basis material images can be simply generated using matrix inversion. However, matrix inversion would yield amplified image noise and lower decomposition accuracy. This problem is the main objective to address in image-domain based material decomposition. We will implement an image-domain material decomposition algorithm to optimize energy combination for the decomposition of cortical bone, soft tissue and gold solution.

Although it is expected that the energy above K-edge of gold is the optimal option, it can't be applied in some small animal experiment since the anatomic structures are not clearly visible at such high energy.

A previous study showed that micro-CT imaging at 40kVp and 80kVp are optimized energy pair to differentiate iodine and gold-based nanoparticles[14]. Based on these results, we will assess all possible combination between 30kVp and 80kVp. In addition, we will employ a 'joint' bilateral filtration [2] for denoising. The rest of this paper is organized as follow. The next section describes the algorithm of dual-energy material decomposition, the experimental design of numerical simulations and the joint bilateral filtration. The third section presents numerical experiment results. The last section discusses some related issues and makes a conclusion for this paper.

II. METHODS

A. Dual-Energy Material Decomposition

In this study, we implement the algorithm developed by Vinegar and Wellington[15] to generate independent images of cortical bone, soft tissue and Au. The algorithm is designed for a three-phase system, at least two independent measurements are needed to determine the fractions. For each voxel of a CT image, the effective linear attenuation coefficient (μ) could be expressed as a linear combination of the attenuation coefficients of basis materials multiplied by their corresponding volume fraction

$$\mu_{CB,E} \cdot f_{CB} + \mu_{ST,E} \cdot f_{ST} + \mu_{Au,E} \cdot f_{Au} = \mu_E \quad , \qquad (1)$$

where $\mu_{CB,E}$, $\mu_{ST,E}$, $\mu_{Au,E}$ are the effective linear attenuation coefficients acquired at a mean x-ray energy E of cortical bone, soft tissue, and the solution of Au, respectively, and $f_{CB}, f_{ST}, and\ f_{Au}$ represent the corresponding volume fractions. If a voxel contains only three basis materials, the sum of these volume fractions has to be equal to 1.

$$f_{CB} + f_{ST} + f_{Au} = 1 \qquad (2)$$

For two CT images reconstructed at mean energies E1 and E2, we have two independent measurements of the attenuation coefficients:

$$\mu_{CB,E1} \cdot f_{CB} + \mu_{ST,E1} \cdot f_{ST} + \mu_{Au,E1} \cdot f_{Au} = \mu_{E1}, \qquad (3)$$

$$\mu_{CB,E2} \cdot f_{CB} + \mu_{ST,E2} \cdot f_{ST} + \mu_{Au,E2} \cdot f_{Au} = \mu_{E2}. \qquad (4)$$

The linear attenuation coefficients for basis materials at each energy can be measured from the CT images within regions known to contain the corresponding basis materials. As a result, the three unknowns $f_{CB}, f_{ST}, and\ f_{Au}$ could be solved. In our implementation, we assumed that the percentage concentration of each of three basis materials (fractions) must be a non-negative and voxels with the linear attenuation coefficients below soft tissue (i.e., air-containing regions) contain no basis materials.

B. Experimental Design

To determine the optimal x-ray tube potential energies (below K-edge of Au) of dual energy decomposition, a 2D phantom (Fig.1a) is designed by following the work of Badea [14]. The phantom contains soft tissue, a cortical-bone-mimicking material (epoxy 32.51% and calcium carbonate 67.49% by weight, a density of 1.84 g/cm^3) and a series of five Au solutions with different concentrations (1 mg/ml, 2 mg/ml, 4 mg/ml,8 mg/ml and 16 mg/ml). The diameters of the 2D phantom and the inserts were 6.0 cm, 1.0 cm and 0.6 cm, respectively. The corresponding values of linear attenuation coefficients are obtained from National Institute of Standards and Technology (NIST) database. The linear attenuation coefficients of the Au concentrations are calculated using the mixture rule, and the attenuation curves of those materials are shown in Fig.1b.

X-ray spectra are significantly influenced by kVp, target material and filtration [15]. The x-ray spectra were obtained from Siemens [20]. The simulated x-ray source includes tungsten and 1.0 mm Al extrinsic filtration. This will increase the mean energy of the high-energy spectrum to be as high as possible and provide adequate photon flux[16].

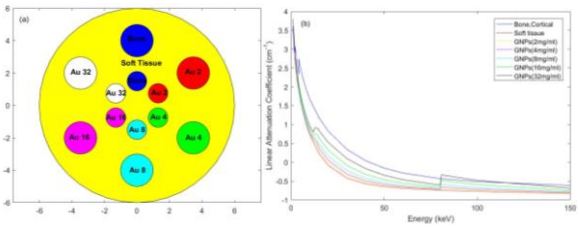

Fig.1. 2D numerical phantom. (a) is the illustration of phantom structure. (b) shows linear attenuation coefficients with respect to incident photon energy of diferent materials, where y axis is plotted on a logarithmic scale.

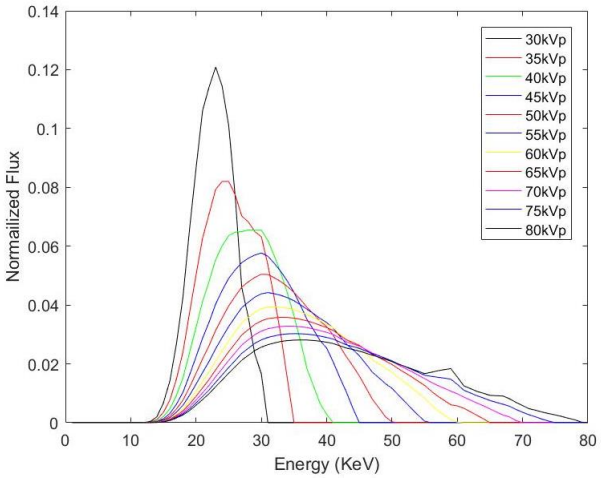

Fig.2. Normalized x-ray spectra for different voltages (30kVp to 80kVp, increment: 5kVp) used in numerical simulation.

The phantom is virtually irradiated to generate projections at each keV. The final pre-log projection for a given kVp is a weighted sum of projections at all keV and the weight is the normalized flux shown in Fig.2. The projections are generated with a step of 5 kVp starting at 30kVp and ending at 80kVp. The exposure intervals for each acquisition are equal and the number of photons is 4×10^5 for each x-ray path. For each experiment, a 2D fan-beam CT geometry was assumed, the distance from the source to the rotation center is 351mm, the distance from the source to the detector is 541 mm, a circular scan is simulated and 720 projections are uniformly acquired. The detector pixel size is 0.0078 mm and the detector includes 1024 pixels. To be realistic, Poisson noise is superimposed into the projection[17]. A conventional filtered backprojection algorithm is employed for image reconstruction. The dual energy material decomposition is performed on reconstructed images with Poisson noise.

The accuracy of the dual energy decomposition is assessed by the relative root mean square error (rRMSE). The decomposition accuracy is calculated for cortical bone image, soft tissue image and Au image, respectively. For one material-specific image, rRMSE is computed as follows:

$$\mathrm{rRMSE} = \sqrt{\frac{\sum_i \left| f_{P,i} - f_{E,i} \right|^2}{\sum_i \left| f_{E,i} \right|^2}} \quad (6)$$

Where $f_{P,i}$ is the value of the i[th] pixel in the basis material image decomposed from reconstructed images with Poisson noise, $f_{E,i}$ is the value of the i[th] pixel in the basis material image decomposed from the ground-truth data obtained from the numerical phantom, and *N* was the total number of pixels in the basis material image.

C. Bilateral filtration

To improve the decomposition accuracy, the reconstructed images are filtered using bilateral filtration (BF) [18] before decomposition. The BF can denoise the reconstructed volumetric images and preserve edges by performing the following operation on each voxel:

$$\mathbf{f}'(\boldsymbol{x}) = k^{-1}(\boldsymbol{x}) \int_{-\infty}^{\infty} \int_{-\infty}^{\infty} \boldsymbol{f}(\varepsilon)\, \mathrm{d}\,(\varepsilon, \boldsymbol{x})\, \mathrm{r}(\boldsymbol{f}(\varepsilon), \boldsymbol{f}(\boldsymbol{x}))\, \mathrm{d}\varepsilon \quad (7)$$

where d ($\varepsilon, \boldsymbol{x}$) measures the geometric closeness between the neighborhood center $\boldsymbol{x}$ and a nearby point ε; $\mathrm{r}(\boldsymbol{f}(\varepsilon), \boldsymbol{f}(\boldsymbol{x}))$ measures the photometric similarity between the pixel at the neighborhood center $\boldsymbol{x}$ and that of the a nearby point ε.The similarity function r operates in the range of the image function **f**, while the closeness function d operates in the domain of **f.** Both d ($\varepsilon, \boldsymbol{x}$) and $\mathrm{r}(\boldsymbol{f}(\varepsilon), \boldsymbol{f}(\boldsymbol{x}))$ are Gaussian functions of Euclidean distance between their arguments as below:

$$\mathrm{d}\,(\varepsilon, \boldsymbol{x}) = \exp\left(-\frac{1}{2}\left(\frac{\|\varepsilon - \boldsymbol{x}\|}{\sigma_d}\right)^2\right) \quad (8)$$

and

$$\mathrm{r}(\boldsymbol{f}(\varepsilon), \boldsymbol{f}(\boldsymbol{x})) = \exp\left(-\frac{1}{2}\left(\frac{\|\boldsymbol{f}(\varepsilon) - \boldsymbol{f}(\boldsymbol{x})\|}{\sigma_r}\right)^2\right) . \quad (9)$$

In this simulation study, for all kVp data, we use σ_d=4 and σ_r=0.1. d ($\varepsilon, \boldsymbol{x}$) is constructed within in a radius of 6 pixels. A new extension of BF ('joint') described by Clark [2] substituted $r_{low} \cdot r_{high}$ for r_{low} and r_{high} , respectively. Here, r_{low} computed range weights using the low-voltage data, r_{high} computed range weights using the high-voltage data. The 'joint' range weights are computed using both voltages data and then each pixel is filtered independently.

$$r_{low} r_{high} = \exp\left(-\frac{1}{2}\left(\frac{\|\boldsymbol{f_{low}}(\varepsilon) - \boldsymbol{f_{low}}(\boldsymbol{x})\|}{\sigma_{r,low}}\right)^2\right) + \exp\left(-\frac{1}{2}\left(\frac{\|\boldsymbol{f_{high}}(\varepsilon) - \boldsymbol{f_{high}}(\boldsymbol{x})\|}{\sigma_{r,high}}\right)^2\right) \quad (10)$$

Obviously, the main advantage of the 'joint' BF is that the same pixel at different energies be used in the decomposition is processed with a consistent filtration.

III. Results

We reconstructed images at different scanning kVp voltage (every 5 kVp, from 30kVp to 80kVp). The reconstructed images at 50kVp and 75kVp are shown in Fig.3. The images of both energies were corrected using a beam hardening bone correction algorithm to remove residual high order beam hardening artifacts (streaks), especially in high attenuation material part, such as bone.

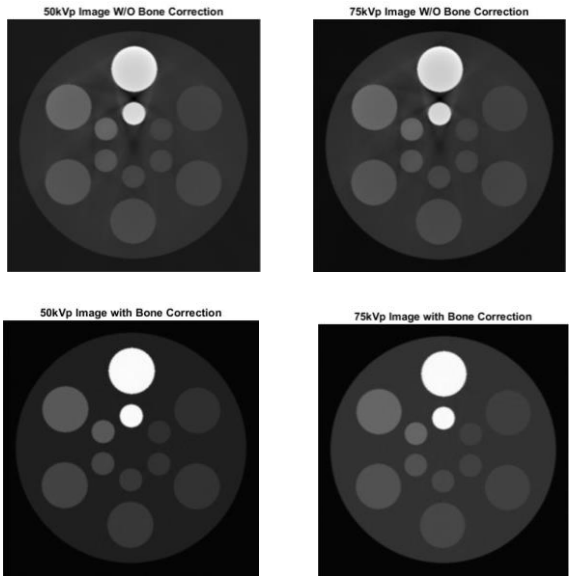

Fig. 3 Image reconstruction results of the numerical phantom simulation. The top row shows the 50 kV and 75 kV CT images. In the bottom row, the beam hardening bone correction had been performed.

Bone, Soft Tissue and the 12 mg/ml Au solution are selected as the basis materials for dual-energy material decomposition. Other Au solutions shown up in the decomposed images correspond to the contribution of their linear attenuation coefficients to the linear attenuation coefficient of the selected basis material.

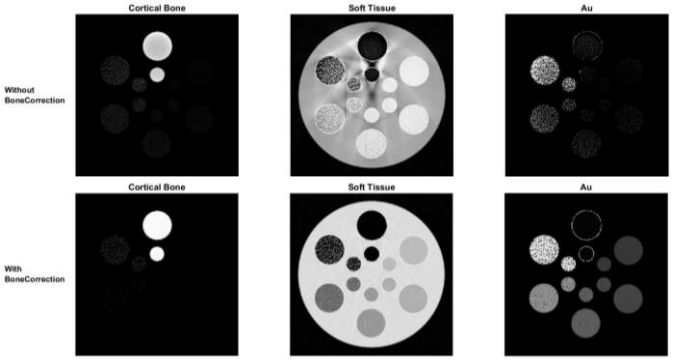

Fig. 4 The decomposed basis material images without and with bone correction.

Fig.4 shows dual-energy material decomposition results using direct matrix inversion with and without bone correction. Obviously, dual-energy material decomposition yields residual cupping artifacts in the basis material images without bone correction, and these basis material images are inhomogeneous. This is because the image-domain matrix inversion just linearly combine the high- and low-energy

images, and does not consider the nonlinear attenuation process of x-ray projection [8].

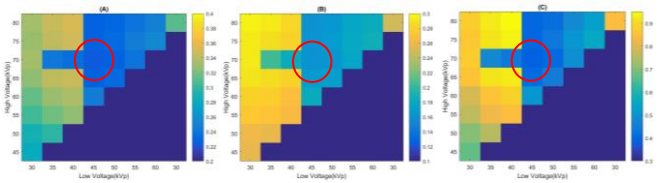

Fig.5. The rRMSE values for all possible combinations of voltages. The minimum difference of two voltages is 3 increments and each increment is 5kVp. (A)- (C) are the rRMSE values of cortical bone, soft tissue and Au, respectively. Base on the rRMSE results, the lowest value can be obtained when the scanning voltages are 45kVp and 70kVp in cortical bone image, soft tissue image and Au image (red circle).

Fig.5 shows the accuracy of the dual energy decomposition for all possible combinations of voltages in the numerical simulations. In Fig.3(A) and Fig.3(C), the lowest rRMSE indicates the optimized combination of voltages between 30kVp and 80kVp is 45kVp and 70kVp. The accuracy is greater than others when the low voltage is 45kVp. The best decomposition accuracies for the cortical bone, soft tissue and Au were 0.2227, 0.1597 and 0.3813, respectively.

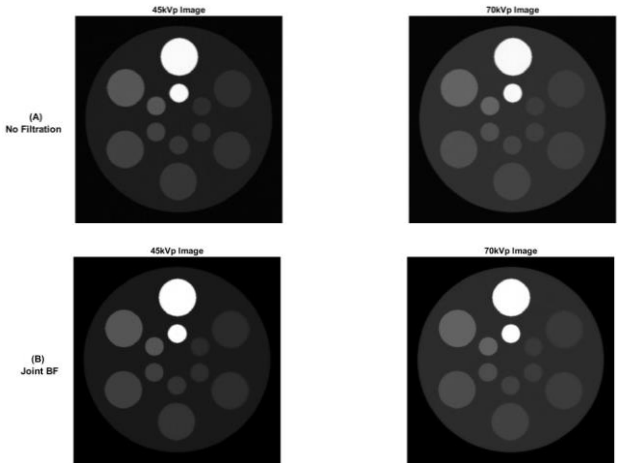

Fig.6. Reconstructed dual energy phantom images at 45kVp and 70kVp from noisy projections.

Fig.6. shows the reconstructed phantom images at 45kVp and 70kVp with Poisson noise before and after filtration with joint BF. Fig.7 displays the material-specific images decomposed from dual energies at 45kVp and 70kVp. More specifically, the first row shows the basis material images obtained by decomposing the reference phantom images from noise-free projections (Fig.7. (A)); the second row shows the counterparts with Poisson noise; the third row shows counterparts with Poisson noise and after joint BF. Based on the rRMSEs, we can see that joint BF improves the decomposition accuracies for cortical bone and Au.

For dual energy decomposition, all images were reconstructed from the projection with Poisson noise. When the low voltage is fixed at kVp, the high voltage is varied from 60kVp to 80kVp, and the rRMSEs are calculated on each decomposed image (see Fig.8). The plots in Fig.8 show that joint BF improves the decomposition accuracies of cortical bone image, soft tissue image and Au image.

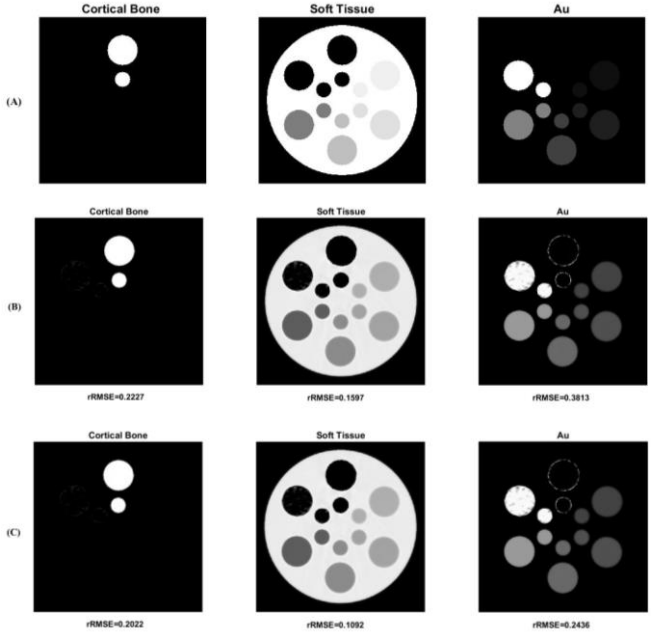

Fig.7. Dual-energy decomposition of the reconstructed phantom images at 45kVp and 70kVp. (A) are material maps decomposed from reconstruction images without noise; (B) are the counterparts with Poisson noise but without joint BF and (C) are the counterparts with Poisson noise and with joint BF.

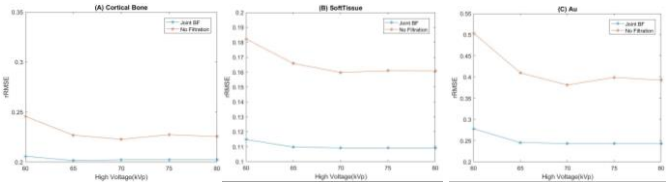

Fig.8. rRMSEs of dual energy decomposition results for fixed low voltage at 45kVp and varying high voltages from 60kVp to 80kVp. In each basis material image, two curves represented the rRMES values with and without joint BF

IV. Discussion and Conclusion

Dual energy CT offers capability for materials differentiation which is vitally important for clinical applications. For instance, it could be used to detect the character of given materials and quantify the corresponding amounts[7]. This study implements an image-domain dual-energy material decomposition algorithm to optimize voltage combination to differentiate cortical bone, soft tissue and gold solution. In our numerical simulation, the voltage combinations are ignored when the difference between two voltages is small than 15kVp because a previous study showed the rRMSE values was higher than others when the difference between two voltages is 10kVp [14]. In this case, the rRMSE results show the optimized voltage combination is 45kVp and 70kVp which provides a basis for *in vivo* small animal experiments. For example, the decomposed gold image could visualize the physiological characterizations of tumor vasculature since

gold can be passively accumulated at the tumor sites. Using the optimized voltage combination below K-edge, both tumor sites perfused with the gold-based contrast agent and anatomical structure of small animals (e.g. nude mice) could be clearly visible. For image-domain dual-energy decomposition algorithm, the technique with direct matrix inversion is easy for understanding and implementation. However, it yields high noise level. Since the intensities between voltages are strongly correlated due to the linear nature of CT contrast, joint bilateral filtration should improve the accuracy of DE decompositions relative to independent filtration[2]. As what we expected, joint bilateral filtration demonstrates its role in smoothing Poisson noise and improving the decomposition accuracy for cortical bone and gold solutions. Different from the joint bilateral filtration introduced by Clark[2], we used a simplified version without medial filtration [19].

This study still has several limitations. First, only numerical simulations were performed to optimize voltage combination and evaluate the effect of joint bilateral filtration. However, more complicated and realistic physical phantoms and *in vivo* small animal experiments have not been performed yet. Second, we validated the effect of joint bilateral filtration for only one noise level. In future, it is necessary to evaluate its stability with respect to different noise levels. Third, we didn't analyze the impact of the concentration of gold solution. Besides, the voltage of x-ray tube and the concentration of contrast agents is also determinant. There is a linear relation between CT enhancement and the concentration of attenuating material. Considering the potential toxicity of gold-based contrast agents, it is crucial to determine the minimal visible concentration in *in vivo* small animal experiments. All those issues will be investigated in the near future.

In summary, image-domain dual-energy material decomposition is a convenient method in clinical applications because it is directly performed on reconstructed CT images the optimized voltages combination and the edge-preserving filtration (e.g. joint filtration) provide an efficient path toward higher accuracy in material decomposition. In near future, we will develop a new joint bilateral filtration based on some correlations of the intensities between the images at two voltages. Meanwhile, numerical experiments at different noise levels and *in vivo* small animal experiments will be performed to further evaluate the robustness of the new method.

ACKNOWLEDGMENT

This work was supported in part by NIH/NIBIB U01 grant EB017140.

REFERENCES

[1] D. Cavanaugh, E. Johnson, R. E. Price, J. Kurie, E. L. Travis, and D. D. Cody, "In vivo respiratory-gated micro-CT imaging in small-animal oncology models," *Mol. Imaging*, vol. 3, no. 1, pp. 55–62, 2004.

[2] D. P. Clark, K. Ghaghada, E. J. Moding, D. G. Kirsch, and C. T. Badea, "In vivo characterization of tumor vasculature using iodine and gold nanoparticles and dual energy micro-CT," *Phys. Med. Biol.*, vol. 58, no. 6, p. 1683, 2013.

[3] J. F. Hainfeld, D. N. Slatkin, T. M. Focella, and H. M. Smilowitz, "Gold nanoparticles: a new X-ray contrast agent," *Br. J. Radiol.*, vol. 79, no. 939, pp. 248–253, 2006.

[4] J. F. Dorsey *et al.*, "Gold nanoparticles in radiation research: potential applications for imaging and radiosensitization.," *Transl. Cancer Res.*, vol. 2, no. 4, pp. 280–291, 2013.

[5] E. E. Connor, J. Mwamuka, A. Gole, C. J. Murphy, and M. D. Wyatt, "Gold nanoparticles are taken up by human cells but do not cause acute cytotoxicity," *Small*, vol. 1, no. 3, pp. 325–327, 2005.

[6] A. Manuscript, *Focus on Micelles*, vol. 9, no. 1. 2015.

[7] P. R. S. Mendonca, P. Lamb, and D. V. Sahani, "A flexible method for multi-material decomposition of dual-energy CT images," *IEEE Trans. Med. Imaging*, vol. 33, no. 1, pp. 99–116, 2014.

[8] W. Zhao *et al.*, "Using edge-preserving algorithm with non-local mean for significantly improved image-domain material decomposition in dual-energy CT," *Phys. Med. Biol.*, p. 1332.

[9] C. Maaß, E. Meyer, and M. Kachelrieß, "Exact dual energy material decomposition from inconsistent rays (MDIR)," *Med. Phys.*, vol. 38, no. 2, pp. 691–700, Feb. 2011.

[10] T. Niu, X. Dong, M. Petrongolo, and L. Zhu, "Iterative image-domain decomposition for dual-energy CT," *Med. Phys.*, vol. 41, no. 4, p. 41901, 2014.

[11] D. P. Clark and C. T. Badea, "Spectral diffusion: an algorithm for robust material decomposition of spectral CT data," *Phys. Med. Biol.*, vol. 59, no. 21, p. 6445, 2014.

[12] S. Mukundan *et al.*, "A liposomal nanoscale contrast agent for preclinical CT in mice," *Am. J. Roentgenol.*, vol. 186, no. 2, pp. 300–307, 2006.

[13] Z. Li, S. Leng, L. Yu, Z. Yu, and C. H. McCollough, " Image-based material decomposition with a general volume constraint for photon-counting CT ," 2015, vol. 9412, p. 94120T–94120T–8.

[14] C. T. Badea, S. M. Johnston, Y. Qi, K. Ghaghada, and G. A. Johnson, "Dual-energy micro-CT imaging for differentiation of iodine- and gold-based nanoparticles," vol. 7961, p. 79611X, 2011.

[15] H. J. Vinegar and S. L. Wellington, "Tomographic imaging of three-phase flow experiments," *Rev. Sci. Instrum.*, vol. 58, no. 1, pp. 96–107, 1987.

[16] P. V. Granton, S. I. Pollmann, N. L. Ford, M. Drangova, and D. W. Holdsworth, "Implementation of dual- and triple-energy cone-beam micro-CT for postreconstruction material decomposition," *Med. Phys.*, vol. 35, no. 11, p. 5030, 2008.

[17] J. Nuyts, B. De Man, J. A. Fessler, W. Zbijewski, and F. J. Beekman, "Modelling the physics in the iterative reconstruction for transmission computed tomography.," *Phys. Med. Biol.*, vol. 58, no. 12, pp. R63-96, 2013.

[18] C. Tomasi and R. Manduchi, "Bilateral Filtering for Gray and Color Images," *Int. Conf. Comput. Vis.*, pp. 839–846, 1998.

[19] D. Clark, G. a Johnson, and C. T. Badea, "Denoising of 4D Cardiac Micro-CT Data Using Median-Centric Bilateral Filtration.," *Proc. SPIE Med. Imaging*, vol. 8314, pp. 1–12, 2012.

[20] https://bps-healthcare.siemens.com/cv_oem/radIn.asp